# A Snapshot Imaging System for the Measurement of Solar-Induced Chlorophyll Fluorescence— Addressing the Challenges of High-Performance Spectral Imaging

Caspar Kneer, Andreas Burkart, Jens Bongartz, Bastian Siegmann, Juliane Bendig, Alexander Jenal, and Uwe Rascher

Abstract—**This article introduces a novel stereo-camera system for the measurement of solar-induced chlorophyll fluorescence (SIF) at 760 nm. The instrument uses optical interference filters to gain high background radiation-suppression in the telluric oxygen absorption band at 760 nm, to measure the weak SIF signal. Featuring spatially high-resolution images and a lightweight setup, the system was built for ground- and drone-based field applications. The technical setup of the device and the used methodology are presented as well as a theoretical performance simulation, indicating a maximal reduction of the background radiation by a factor of five. The experimental results show that steady-state fluorescence can be measured with signal-to-noise ratios (SNRs) between 5 and 10, depending on the saturation level of the sensor and the aperture settings of the lens. Intensity changes lower than 0.2 mWm^{-2}sr^{-1}nm^{-1}, emitted by a calibrated light emitting diode (LED) reference panel, can be reliably distinguished under direct sun illumination. The system's capability to detect fast changes in photosynthetic dynamics, with both high spatial and temporal resolution, is demonstrated by a video sequence of a leaf during a dark-light transition. In a static, platform-based operation, the classification of fluorescent and nonfluorescent surfaces under natural conditions is presented.**

Index Terms— **Camera-based solar-induced chlorophyll fluorescence (SIF) measurement, photosynthetic dynamics, remote sensing of vegetation, SIF.**
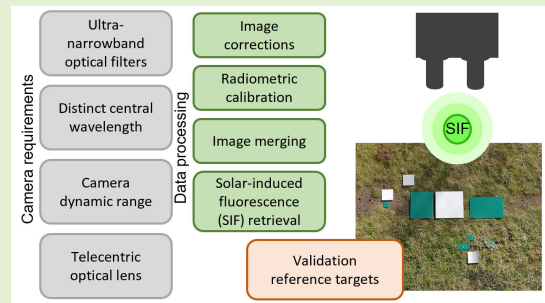
I. INTRODUCTION

SOLAR-INDUCED chlorophyll fluorescence (SIF), is directly linked to photosynthetic activity and has

recently become a major research topic in remote sensing of vegetation. Its origin in the photosystems makes it the only remotely measurable signal, that is directly emitted by plants and thus can provide a good estimation of photosynthetic activity. Chlorophyll fluorescence is, together with heat dissipation and the absorption of photon energy for photosynthesis, one of the ways plants channel the absorbed incoming light. As those pathways are competitive, the SIF signal reveals an inversely proportional linkage to photosynthetic assimilation [31]. However, the magnitude of the signal is very low compared to solar irradiation and the amount of light vegetation reflects. The contribution of the SIF emission to the total radiation released from plants is around 1%–3%, while the amount of reflected light in the near-infrared (NIR) spectral domain, in which

the SIF signal is emitted (650–800 nm), is around 50% of the sun's total irradiance reaching the surface. Steady-state fluorescence with an approximated radiant flux of about 1–2 $mWm^{-2}nm^{-1}sr^{-1}$, at its two peak wavelengths 685 and 740 nm, is therefore highly superimposed by the reflected radiance of vegetation [24], [25]. To disentangle SIF and reflected radiation under natural light conditions, the radiative transfer through the atmosphere has to be precisely acknowledged, i.e., scattered ambient light and angular dependencies, like the bidirectional reflectance distribution function (BRDF) [8], [39].

Various instruments and methods have been developed to retrieve chlorophyll fluorescence (F), which can be differentiated, based on whether they are active or passive, on the scale of the application, the used light source, or the spectral and spatial resolution of the output data. Leaf level systems like the fluorescence leaf-clip FluoWat [2] as well as laboratory microscope systems and active pulse-amplified modulation (PAM) fluorometer [3] benefit from the advantage of precise control of the excitation light. In remote sensing at-canopy level, where SIF is mainly measured, this advantage does not apply.

Therefore, various passive instruments have been developed. For ground-based measurements a number of high-grade point-spectrometer systems are available, like FloX [9], SIFSpec [10], FluoSpex [38], Piccolo [19], FAME [14], and PhotoSpec [13]. Furthermore, some point-spectrometer systems are lightweight enough to be mounted on unmanned aerial vehicles (UAVs), namely, Piccolo Doppio [22], AIR-SIF [6], [7], and AIRFLOX [37]. In 2004, Moya et al. [27] introduced a dual-channel system combining interference filters with photodiodes to measure SIF. The further development of this three spectral channel system called Airflex was tested in an airborne experiment in 2006 [26]. Moreover, there are imaging spectrometer systems, like CFIS [12], HyPlant [32], [35], and FIREFLY [29], operated mainly on larger aircraft due to the weight factor, power requirements, and additionally needed instruments, e.g., inertial navigation systems. According to our knowledge, up to now, no validated imaging system uses snapshot cameras for the measurement of SIF reported in the literature, that is compact enough to be carried by a UAV.

This article discusses the possibilities of combining optical interference filter, narrow enough to sample the O_2A absorption band sufficiently, with an imaging lens that produces a reasonable field of view (FOV), but with special regard to image-side field and cone angles. Furthermore, this study is evaluating the question, if this combination can suppress the reflected sunlight adequately so that a high dynamic range (DR) camera can resolve the remaining portion of emitted fluorescence. In Section II, the used materials and methods as well as the technical requirements and implementations for a snapshot-imaging SIF system are presented. To evaluate the performance of the camera system under bright sunlight conditions, four experiments were conducted and are introduced in Section III. In the first experiment, the general capability of the camera system to discriminate the weak

fluorescence emission from high background radiation was investigated. A tuneable and radiometrically calibrated light emitting diode (LED) target was used to test the system's signal resolution and the influence of different aperture settings and sensor saturation levels. In a second experiment, the SIF of a vegetation surface was measured. During the experiment, several images of a philodendron leaf were recorded under direct sun illumination. A part of the leaf was covered for about 30 min to stimulate dark adaption. After removing the cover and exposing the leaf to direct sun light, the Kautsky effect [16] was clearly visible, which is characterized by an increased SIF emission followed by a decay to a steady-state level. The third experiment aimed to investigate the capabilities of the camera system for mid-range (approximately 9 m) measurements of reflectance and fluorescence targets in natural surroundings from a phenotyping platform. Experiment four shows an example of data from the camera system mounted on a UAV and a comparison with reference SIF collected on the ground.

## II. CHALLENGES TO MEASURE SIF WITH A SNAPSHOT CAMERA SYSTEM

Recently, SIF measurements are performed using high resolution and high DR point- and scanning-spectrometers. Nevertheless, most of those systems are still not able to separate the full fluorescence spectrum from vegetation-reflected radiation due to signal-to-noise ratio (SNR) limitations. According to [13] and [28], the ideal requirements for measurements of the full SIF spectrum would be a high spectral resolution (full width at half maximum (FWHM) <0.4 nm), a high maximal SNR ($\geq$1000:1) and an extended DR (>16 bit).

Therefore, methods have been developed that try to reduce the impact of those limitations and bypass the problems introduced by the high amount of background radiation. Those methods are summarized under the term Fraunhofer line discriminator (FLD) [15] and were originally considered for measurements inside the narrow Fraunhofer absorption lines in the solar spectrum. Moreover, the principle of the FLD method can be used for measurements inside the wider telluric oxygen absorption bands, introduced by Earth's atmosphere. The Sun's ground level radiance in the O_2A (760 nm) and O_2B (687 nm) bands is approximately ten times lower than the radiance outside the bands, depending on the spectral resolution of the measurement instrument. The amount of background radiation inside those bands is drastically reduced, while the amount of the emitted fluorescence signal stays unchanged.

A. Principles of the FLD Method

To discriminate SIF from incoming radiance the FLD method is used. Fig. 1 shows the O_2A band at 760 nm and the two wavelength bands λ_{in} and λ_{out} (green) with the derived FLD parameters for radiance (Rad_{in} and Rad_{out}) and irradiance (Irr_{in} and Irr_{out}). Using (1), the emitted fluorescence of a target, overlying the measured at-sensor radiance, can be calculated

$$F = \frac{Rad_{in} \times Irr_{out} - Rad_{out} \times Irr_{in}}{Irr_{out} - Irr_{in}}. \tag{1}$$
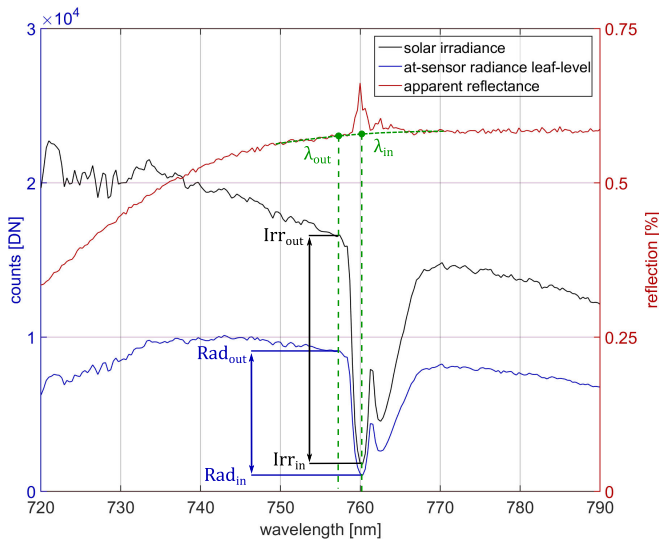
Fig. 1. Solar irradiance at reference target (black) and radiance of a green leaf (blue) with highlighted FLD parameters for the two wavelengths λ_{in} and λ_{out} (green). Calculated reflectance (red) with comprehended fluorescence fraction and characteristic peak at 760 nm, caused by infilling of the O_2A absorption band.

Fig. 2. Visualization of emanating ray-bundles for the calculation of sensor-position, aperture, and exit pupil position dependent filter transmission profile degradation. For a better visibility, just the outer radius and a reduced number of rays as well as the chief rays (blue) are shown. The original number and distribution of rays can be seen in the pupil sampling plot. The transmission profile plot shows simulated data for the two spots on the image sensor at $f/8.0$ and the primary filter profile for AOI 0°.

Equation (1) is fulfilled if assuming that both reflectance inside ($Refl_{in}$) and outside ($Refl_{out}$) the absorption band, as well as the fluorescence inside (F_{in}) and outside (F_{out}) the band are equal
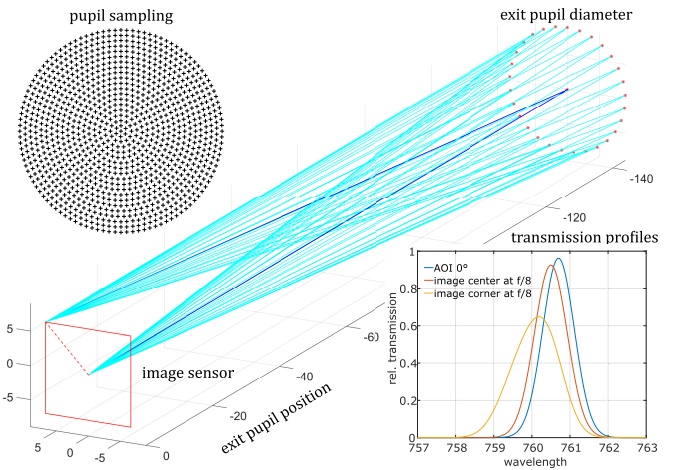
$$Refl_{in} = Refl_{out} \quad F_{in} = F_{out}. \tag{2}$$

It can be seen from Fig. 1 that the first assumption regarding the reflectance inside and outside the band is nearly true for vegetation, provided that reflection in the considered wavelength range is continuous. Therefore, methods like 3FLD [21] or iFLD [1] use sampling points on the left and right shoulder around the O_2A band to approximate expected reflectance from apparent reflectance, as is indicated with the green dashed line in Fig. 1.

For a camera-based measurement of SIF using the FLD method at least two spectral channels are needed, one sampling Rad_{in} and Irr_{in} and one Rad_{out} and Irr_{out}. The system described in this article is based on two cameras, each equipped with an optical bandpass filter for the spectral channel separation, hereinafter named the inside band camera (IBC) and the outside band camera (OBC).

B. Filter Requirements—The Challenge to Use Ultra-Narrowband Optical Filter for High-Resolution Spectral Imaging

In Section II-B some considerations regarding the usage of off-the-shelf ultra-narrowband interference filters in proximal sensing applications, and the combination of those with nearly image-side telecentric lenses, are presented. A MATLAB (The MathWorks Inc., Natick, MA, USA) simulation was developed, which allows to calculate the distribution of filter bandwidth (BW) and central wavelength (CW) over the focal-plane dimension for a given lens-filter-sensor combination. As a general rule, interference filters are designed for use with collimated light and small ranges of angles of

incident (AOI). The filters used in this work are specified for AOI = 0° with an angle tolerance of ±4°. For the IBC a CW of 760.7 nm is used with a FWHM of <1.2 nm, for OBC the CW is 757.9 nm also with <1.2 nm FWHM. Both filters have a wide blocking range (200–1200 nm) with an optical density (OD) of 4 and a peak transmission of >90% for their particular CW. If those filters are exposed to light with higher incident angles, their spectral characteristics will start to change and the transmission degrades [20]. For most interference filters a spectral shift toward shorter wavelengths can be observed, depending on the deviation from specified AOI. Furthermore, a converging beam, as introduced through an imaging lens, will not only shift the CW but also broaden the transmission band [17], [30]. For the filters, placed between lens and sensor, the modified transmission profiles relative to aperture and sensor position were simulated, according to [34].

The wavelength shift for interference filters caused by nonnormal incident angles θ and for use in the air can be calculated with

$$\lambda_\theta = \lambda_0 \sqrt{1 - \frac{\sin \theta^2}{n_{eff}^2}} \tag{3}$$

with an effective refractive index $n_{eff} = 1.947$ and the CW λ_0 for the particular filter. The filter transmission profile at AOI 0° is approximated using a parametrized probability density function (4) with empirically derived parameter $\varsigma = 0.172$ and wavelength vector λ

$$f(\lambda, \lambda_0, \varsigma) = \frac{1}{\sqrt{2\pi}\varsigma} e^{-\frac{(\lambda-\lambda_0)^2}{2\varsigma}}. \tag{4}$$

In the next step, the exit pupil diameter for a desired aperture setting is calculated and the given circular pupil plane is sampled using polar coordinates, to achieve the starting points for every cone-ray. Fig. 2 shows the geometrical context of
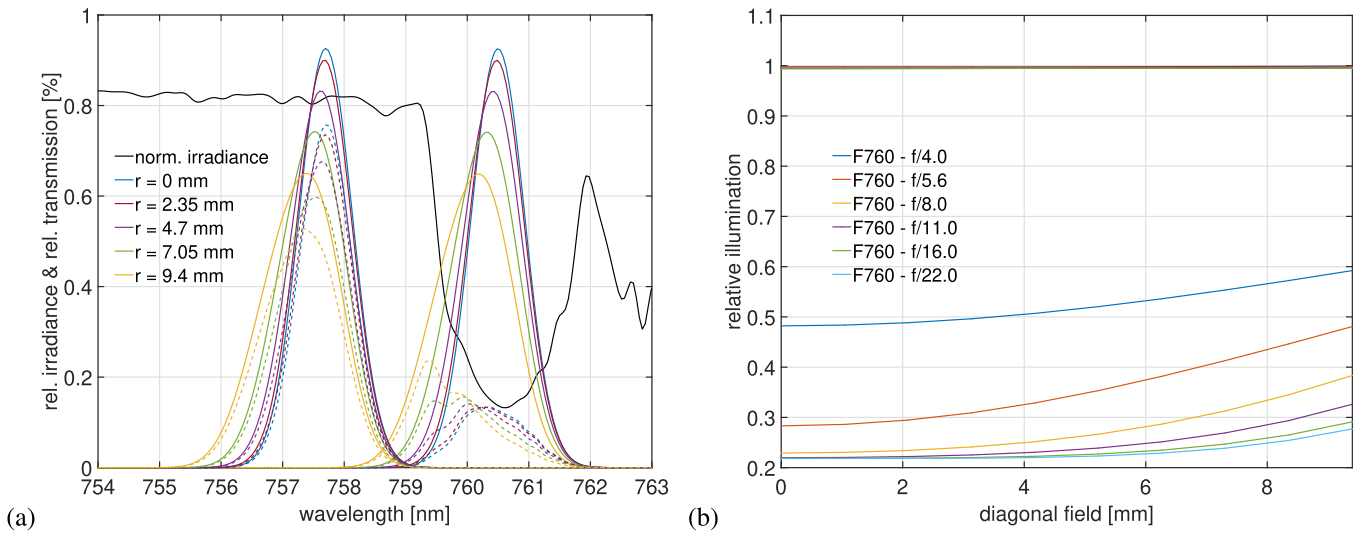
Fig. 3. (a) Simulated transmission profiles for both channels at $f/8.0$ and five steps along the sensor semidiagonal. Dashed lines represent the convolution with the normalized irradiance, in the meaning of transmitted photon energy. (b) Normalized numerical integral over transmitted photon energy relative to the diagonal field for different aperture settings. Horizontal lines at around 100% relative illumination correspond to OBC data and are not stated in the legend.

the pupil diameter, pupil position, and image sensor as well as pupil sampling function.

The calculated ray-angles were used together with (3) to derive the shift of the CW for every ray, and after that, with (4), the corresponding transmission profile. As the number of emanating rays of every radius on the pupil-plane is proportional to the spatial increase of every radius increment, the overall transmission profile for each point at the image-plane corresponds with the average over all single-ray transmission profiles. The former mentioned shift of the CW together with a broadening of the passband and reduction of peak transmission is visible. The effect of filter transmission profile degradation on image illumination is shown in Fig. 3(a).

Continuous lines in Fig. 3(a) show the transmission profiles for both spectral channels at $f/8.0$ and five positions along the semidiagonal image field. Dashed lines are related to the convolution of every profile with normalized irradiance and thus are corresponding to transmitted photon energy. The numerical integral over these curves, as illumination would appear for the imaging sensor, are shown in Fig. 3(b) relative to the diagonal field and for various aperture settings. All data are normalized to the maximum value of the OBC. Note that filter degradation has no impact on relative illumination for the OBC, as the decrease in peak transmission is compensated through the widening of the passband. Therefore, OBC data comply with a horizontal line showing nearly no dependence on field position and aperture. For the IBC, a strong dependence on both aperture and diagonal field position is visible. Thus, we expect a strong impact of the aperture setting on the overall relative signal as well as the illumination homogeneity. It is worth mentioning, that the relative illumination for the IBC indicates brighter image corners than the image center [see Fig. 3(b)], which is a contrary effect to normally occurring lens vignetting.

C. Requirements for Sensitivity, SNR, and DR of the Detector

As described earlier, the steady-state fluorescence signal of natural vegetation contributes just a very small portion to the overall measurable at-sensor radiance. For the O_2A band sampled at very high spectral resolution (<0.5 nm), a portion of around 7%–8% SIF is reported in [25]. Regarding prior considerations, the achievement of such narrow BW with optical filters in combination with entocentric lenses, while preserving the location and width of the passband, seems not possible. The question is, how much suppression of background radiation is actually necessary to disentangle SIF from reflected radiance under natural illumination conditions. An often-used parameter for the assessment of signal-resolving capability is SNR. To assess the dependence of the SNR on DR and saturation of the sensor as well as a relative signal contribution, two exemplary state-of-the-art complementary metal-oxide-semiconductor (CMOS) sensors were compared. A 12-bit CMOS sensor featuring a full well capacity of 10.5 ke⁻ and a 16-bit scientific-CMOS (sCMOS) sensor with 45 ke⁻, respectively. Noise fraction was calculated by including read-(N_R), dark-(N_D), and shot-noise (N_S), while disregarding fixed-pattern-noise (N_{FP}) and photon response nonuniformity (PRNU)

$$N_{\text{total}} = \sqrt{N_R{}^2 + N_D{}^2 + N_S{}^2}. \quad (5)$$

Noise components N_R and N_D were taken from sensor data sheets while N_S equals the square root of the number of photons, due to Poisson statistics. SIF signal S_{SIF} is supposed to be a fixed portion (1%–5%) of the simulated radiance. SNR is calculated as the unit-less ratio of S_{SIF} and N_{total} without using logarithmic scale (dB) as stated as follows:

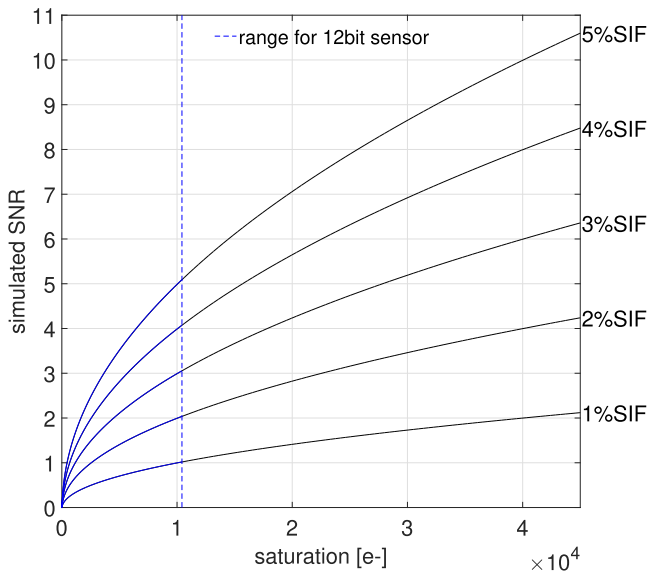$$\text{SNR} = \frac{S_{\text{SIF}}}{N_{\text{total}}}. \quad (6)$$

Fig. 4. Simulated SNR for two exemplary CMOS image sensors relative to the accomplished saturation level and percentage of SIF. Blue lines represent the range of a 12-bit CMOS sensor with a full well capacity of 10.5 ke⁻ while black lines stand for a 16-bit sCMOS sensor reaching 45 ke⁻.

In Fig. 4, a basic simulation of the expectable SNR relative to sensor saturation level is shown. Different lines represent different percentages of SIF to the overall signal.

The dependence on narrow band sampling for achieving reliable fluorescence measurements can be seen from the 1% SIF-line, which corresponds approximately to the outside band signal fraction, as apparent for the OBC. Even the 16-bit sensor at full saturation achieves just an SNR of two, while the 12-bit sensor cannot distinguish signal from noise at all. It can be concluded from Figs. 3(b) and 4 that a practical system will always be a tradeoff. On the one hand, the high aperture closure results in a higher SIF signal ratio and a more homogeneous illumination of the whole sensor area, but with the drawback of much longer integration times. And on the other hand, the saturation level of the sensor has to be considered, which is also depending on the integration time for a fixed amount of light and the quantum efficiency of the sensor. Therefore, the filter parameter CW and BW as well as the DR of the camera are linked together, for this particular application. The narrower the BW of the filter is and the more it fits in the O_2A absorption band, the higher is the percentage of SIF contributed to the measured signal and the lower the camera's DR could be.

D. Hardware Components

The developed system contains two 16-bit sCMOS cameras. Both cameras were equipped with ultra-narrowband interference filters to perform the required spectral separation and suppression of unwanted background radiation. Table I shows a selection of the most important camera and imaging parameters for the combined lens-filter-sensor setup.

The filters were combined with two 25 mm fixed-focal length c-mount objective lenses with a starting aperture of $f/1.8$. Furthermore, the selected lenses show a nearly

TABLE I
CAMERA AND OVERALL SYSTEM PARAMETERS

camera	resolution (full)	2048 x 2048
	sensor size [mm]	13.3 x 13.3 / 18.8 (diag.)
	dynamic range [dB]	87
	binning	2x2, 4x4
system	FOV (full) [deg]	29.8° (hor. & ver.) / 41.2° (diag.)
	storage [GB]	SSD: 500 / microSD: 128
	power consumption [W]	36 max.
	weight [kg]	1.89

Fig. 5. SIF dual-camera system mounted on a DJI Ronin MX gimbal, capable of powering cameras via additional gimbal battery.

image-side telecentric optical path, which is to be considered of major importance for the particular case. All parts were integrated with a dual-camera setup using a computer numerical control (CNC)-machined aluminum plate as the main structural component.

The plate assures torsion stiffness and aligns both cameras' viewing angles precisely. In addition, the plate functions as the heat sink, since the cameras are thermally coupled. Camera control and storage are realized with a built-in single-board computer with an integrated microcontroller co-processor and solid-state drive. The microcontroller is used to generate an external trigger signal for operations where continuous triggering is required, e.g., UAV applications or long-term measurements. The hardware trigger ensures precise synchronization of both cameras' exposure starts, especially necessary when both cameras are operated with different integration times. All other structural components, e.g., holders for computing units and cables as well as the housing are 3-D-printed to guarantee a lightweight design. The housing holds a variety of connectors, e.g., USB type-C and HDMI for video signal, USB-A for connecting external input devices, a connector for power supply, and a microSD card for fast access to stored data. Fig. 5 shows the camera system integrated in a gimbal.

In this setup, the power supply is realized by an additional gimbal battery. To adjust measurement settings, a touch display can be connected to the integrated computing unit.

E. Data Processing, Calibration, and Corrections

The cameras' output is 16-bit grayscale images in tagged image file format (TIFF). All required image processing steps and further calculations for experimental analysis were performed via MATLAB. The postprocessing toolchain, required for the final calculation of SIF using the FLD method, contains the following steps.

1) *Dark Current Correction:* Pixelwise subtraction of an averaged set of at least five to ten dark images, recorded instantaneously before every measurement using the same integration time. For longer experiments, sensor temperature profiles can be recorded.

2) *Distortion Correction:* Lens barrel distortion is removed using a standard approach and empirically determined coefficients. This step is mainly necessary for experiments with short object distances, as otherwise image merging will lead to poor results.

3) *Flatfield Correction:* Can be performed to reduce illumination inhomogeneities introduced by the lens, like vignetting but also due to the angle-dependent filter transmission. Therefore, flatfield correction data have to be recorded under sunlight conditions, e.g., by using Lambertian reference panels.

4) *Radiometric Calibration:* Calibration data were generated with an integrating sphere (1200C-SL, Labsphere, North Sutton, NH, USA).

5) *Image Merging:* Registration and merging are done using control point-based geometric transformation functions from the MATLAB image processing toolbox.

6) *SIF Retrieval:* In-scene radiometry is adjusted with a linear fitting approach (empirical line method (ELM), [36]) using ZenithLite calibration standards (SphereOptics GmbH, Herrsching, Germany), which consist of four, five, or nine fields having different reflectance factors. In addition, this approach is used to derive the apparent irradiance, required for the FLD method. SIF is calculated in (1).

F. LED Reference Panel and Dye Fluorescence Targets

One of the major challenges in evaluating an imaging system to measure SIF is the lack of standardized chlorophyll fluorescence targets. For the presented experiments, we used two custom-made SIF references, an active LED-panel and a passive target painted with fluorescent dye.

1) Active LED Reference Panel: An artificial fluorescence light source was used to perform reliable and repeatable measurements of the SIF signal under direct sun illumination, without the drawback of changing SIF emissions due to changing photosynthetically active radiation (PAR) throughout the day, angular effects like BRDF or inhomogeneities introduced by natural vegetation like a direct reflection of the epidermis [9]. The active panel consists of a matrix of LEDs with emission peaks at 680 and 745 nm and FWHM of 30 nm to mimic the characteristic SIF emission curve.
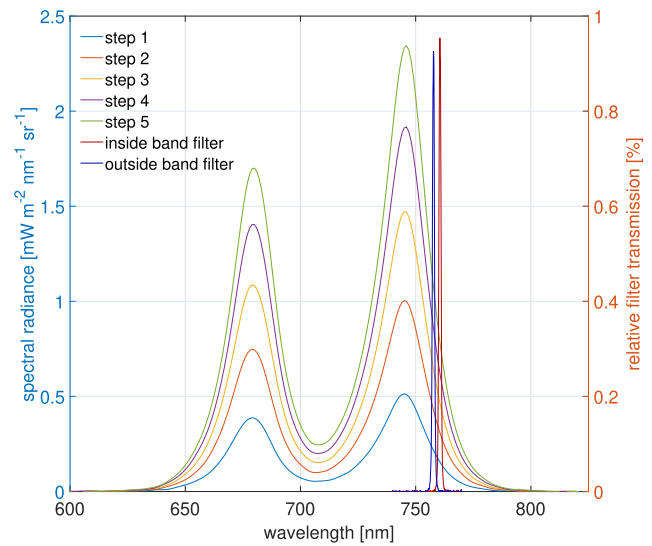

Fig. 6.   Spectral radiance data for the five emission levels of the LED-panel measured with an ASD-FieldSpec 4 spectroradiometer. Relative filter transmission at AOI 0° as reported by the manufacturer.

The LED-matrix is covered with multiple layers of optical diffusor material to provide a nearly Lambertian emission signal. The panels' emission intensity, which is controlled by a microcontroller board via pulsewidth modulation (PWM), can be adjusted in five steps by external buttons. In Fig. 6, the spectral radiance of the panel measured with 1 nm spectral sampling interval using an ASD-FieldSpec 4 spectroradiometer (Analytical Spectral Devices, PANalytical B.V., Boulder, CO, USA) is shown. Furthermore, it is possible to separately trigger the two different wavelength LEDs, to simulate the more complex spectral fluorescence emission of vegetation from photosystems I and II.

2) Passive Dye Fluorescence Target: The dye targets were developed for the 2019 FLEXSense campaign by the Fondazione per il Clima e la Sostenibilità (FCS), Florence, Italy. They are made of wooden boards, which have a green coating on both sides. The coating imitates the characteristic reflectance spectrum of vegetation. One side is additionally coated with special pigments that mimic the SIF emission signal. The advantages of those targets are, besides the size and uniformity of the surface, that they emit SIF without being influenced by living specimen properties (e.g., plant conditions and stress). Unfortunately, the fluorescent dye degrades over time if exposed to ultra violet radiation. This aspect has to be considered for long-term measurements or if the same targets should be used in multiple experiments.

G. SNR Estimation in Presence of Interference Effects

During several experiments, mainly near-field measurements using sunlight in combination with reflectance targets (see Section III-A and III-B), we recognized a pattern in both IBC and OBC images. Primarily interpreted as noise, further investigations showed that the pattern is time- and spatial-invariant, as long as a sensor and target position is not changed. It can be seen that the spatial clustering of the pattern exceeds pixel level, a behavior that would not be expected for any

TABLE II
OVERVIEW OF EXPERIMENTAL SETTINGS: INTEGRATION TIME, SENSOR BINNING FACTOR, MEAN, AND STANDARD DEVIATION OF THE INCOMING RADIANCE MEASURED FROM 50%-REFLECTANCE FIELD OF THE TARGET. IRRADIANCE VALUES IN ROW MEAN(I.) REPRESENT THE MEASURED COUNTS OF THE REFERENCE PANEL AVERAGED OVER THE RECORDED SERIES OF IMAGES. THE ROW STD(I.) REPRESENTS THE STANDARD DEVIATION OF THE 35 IMAGES OF EVERY DATASET. DOUBLE LINES SEPARATE THE DATA IN SETS WHICH WERE RECORDED TOGETHER WITH FOCUS ON CONSISTENT CONDITIONS. DUE TO WEATHER AND SUN ANGLES, DATA WAS RECORDED OVER SEVERAL DAYS, THEREFORE DATA FOR $f/8.0$ WERE RECORDED IN EITHER THE $f/4.0 - f/8.0$ AND $f/8.0 - f/16.0$ IMAGE SERIES

channel	OBC: 757 nm						IBC: 760 nm					
f/#	$f/4.0$	$f/5.6$	$f/8.0$	$f/8.0$	$f/11.0$	$f/16.0$	$f/4.0$	$f/5.6$	$f/8.0$	$f/8.0$	$f/11.0$	$f/16.0$
int. T [ms]	39	82	158	108	205	410	26	352	220	485	250	500
binning	-	-	-	-	-	-	2×2	-	2×2	-	2×2	2×2
mean(I.)	41982	42622	42778	33781	33729	33955	41678	43519	42589	35921	36667	35986
std(I.)	55	66	45	126	52	21	62	71	34	48	49	99
max. rel. S. [%]	0.52	0.61	0.49	0.49	0.61	0.29	1.18	1.74	2.31	2.01	2.09	2.07
sat. level	half		three-quarter		full		half		three-quarter		full	
int. T [ms]	33		51		63		170		255		320	
binning	2×2		2×2		2×2		2×2		2×2		2×2	
mean(I.)	21996		32791		41255		23750		35254		44016	
std(I.)	27		42		40		27		42		33	
max. rel. S. [%]	0.49		0.48		0.55		1.98		1.92		1.79	

kind of noise, except fixed pattern noise. This fixed pattern is related to speckle effects, which mainly occur in near-field experiments when surfaces of fine roughness are measured (e.g., Lambertian reflectance targets). The main reasons for the appearance of those interference effects in the presented experiment are considered to be the narrow BW of the imaging system combined with partial coherence of sunlight and short object-distances [23]. It is worth noting that the statistical influences of those speckle patterns are negligible as long as values are averaged [e.g., for evaluated region of interests (ROIs)]. If standard deviations are calculated from ROIs to asses noise or image inhomogeneities, those patterns introduce a significant error, the speckle contrast. In Sections III-A–III-C, the apparent noise level is therefore defined as the standard deviation σ of a reference ROI from the subtraction of two consecutively captured images Im1 and Im2, divided by $\sqrt{2}$. This is because the noise of two images, such as different noise components [see (5)], add in quadrature. The signal fraction for SNR_{diff} calculation corresponds to the spatial average of the ROI for one of the images Im1 or Im2

$$\text{SNR}_{\text{diff}} = \sqrt{2} \frac{\overline{\text{ROI}_{\text{Im1}}}}{\sigma(\text{ROI}_{\text{Im1}} - \text{ROI}_{\text{Im2}})}. \qquad (7)$$

Equation (7) follows the definition in [11] for the determination of combined read- and shot-noise within images, canceling out any fixed-pattern component.

III. PERFORMANCE EVALUATION OF THE CAMERA SYSTEM

A. Experimental Study I: Measuring SIF Using Controlled Reference Panels

The experiment was conducted to test the systems' ability for resolving very small changes in radiance while a huge background signal is present. The impact of different aperture settings and sensor saturation levels was investigated. At the time the experiment took place, no radiometric calibration data for the cameras were available. Hence, the derived signal from IBC and OBC are stated in digital numbers and compared with the emitted radiance of the panel in $\text{mWm}^{-2}\text{nm}^{-1}\text{sr}^{-1}$.

1) Experimental Setup: The measurements with the active fluorescence panel were performed in April 2020 at noon under the clear sky and direct sun illumination. Cameras were facing in the nadir direction and were mounted at a distance of 1.5 m above the target. To control illumination conditions and enable postcorrections of possible illumination changes of the recorded images, a ZenithLite reference standard consisting of four stripes of varying reflectance factors (90%, 50%, 20%, and 5%) was placed next to the LED-panel in the FOV of the cameras. Aperture settings varied from $f/4.0$ to $f/16.0$ for both cameras. The scene was slightly defocussed and integration times were set to meet at least three-quarters of the camera's DR using a histogram viewer. For investigating the different saturation levels of both cameras, the aperture was set to $f/11.0$ and images with half, three-quarter, and full saturation were recorded. A detailed overview of integration time, sensor binning and the stability of irradiance during the different experiments is provided in Table II.

For better comparability, images for IBC and OBC were recorded successively, to ensure similarity in viewing angles. Using the described setup, 35 manually triggered images were recorded with each camera for the different aperture and dynamic settings. Each image dataset consisted of five dark images, five images of the scene with turned-off LED-panel and five images for the different LED emission intensities.

2) Data Processing: After the measurement, the images were dark-corrected and the relation in reflected radiance between the ZenithLite-Target (50%) and the turned-off LED-panel was analyzed, using average values of equally sized ROIs located close to the image center. This analysis was done to correct for small variations in irradiance
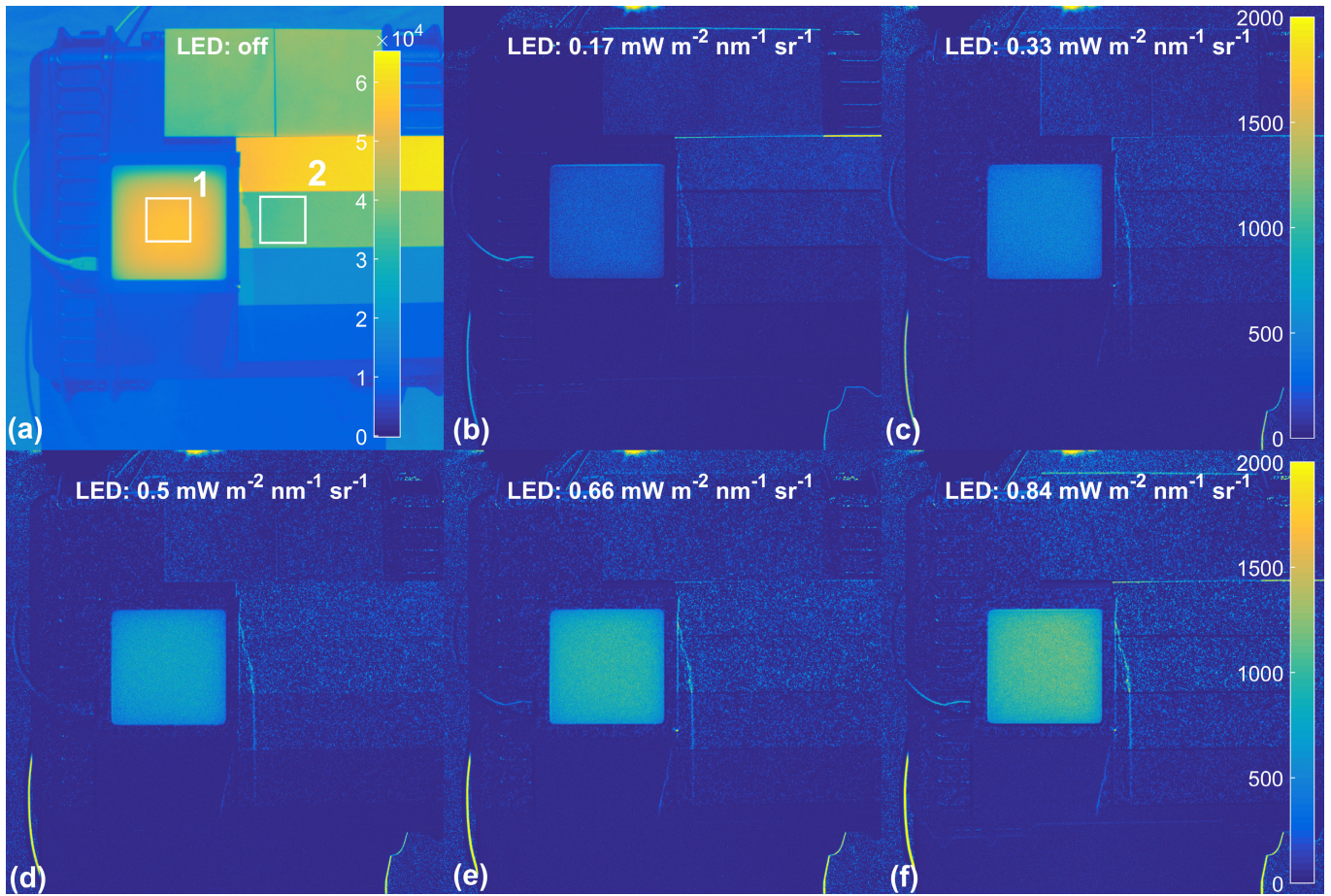
Fig. 7.   (a) Averaged at-sensor-radiance for IBC with selected ROIs (1 and 2). (b)–(f) Averaged difference images for every emission intensity of the LED-panel and the averaged image with turned-off LED-panel. The units of the color bars are in digital numbers.

(e.g., atmospheric changes) during image data acquisition. The image set was averaged and difference images were calculated for each LED emission intensity and the turned-off LED image.

3) Results: Fig. 7(a) shows the averaged at-sensor radiance image of the IBC using an aperture of $f/8.0$ and 485 ms integration time.

The five difference images [Fig. 7(b)–(f)], for each emission intensity of the LED-panel, can be used as an indicator of the resolvable counts for a known amount of radiation. The increase in emission of the LED-panel can be clearly distinguished. The granular pattern apparent in the background of Fig. 7(b)–(f) does not refer to noise, but speckle pattern, as explained in Section II-G. Due to small movements of the LED-panel, introduced while manually triggering the button for adjusting the emission intensities, it could not be excluded that slightly different speckle patterns were combined due to the calculation of different images. The effect of the lens aperture on the resolvable signal is shown in Fig. 8(a) and (b). The graphs show the mean and standard deviation calculated for the different aperture values ($f/4.0$, $f/5.6$, $f/8.0$, $f/11.0$, and $f/16.0$) for the IBC (760 nm) and OBC (757 nm), respectively.

It can be seen that the number of resolvable counts from the measurements inside the absorption feature strongly depends on the used lens aperture for the range between $f/4.0$ and $f/8.0$. Moreover, the higher lens closure resulted in lower variances between the images apparent in the form of lower standard deviations. The results follow an expected distribution as the widening of the filter transmission profile depends on the angles of incidence on the filter. Lower aperture values allowed for higher cone angles and resulted in a wider passband exceeding the narrow O_2-A absorption feature. Thus, more light from the left shoulder of the absorption feature is transmitted and the relative amount of the SIF signal in relation to the overall detected radiance decreased. For aperture values higher than $f/8.0$ no noticeable improvement of the filter transmission profile for IBC was found [see Fig. 8(b)]. This observation may only apply to the examined area of the images covered by the ROIs. For image areas further away from the center, there might be an improvement in signal resolution [see Fig. 3(b)]. Comparison between $f/8.0$ measurements from Fig. 8(a) and (b) revealed a difference of around 200 counts, originating from varying saturation levels and illumination conditions between the two measurements (see Table II). The effect of aperture-closing had no or just a slight effect on OBC signal resolution. Following the prior explanation, a widening of the filter profile also occurred, but had no remarkable influence on the relative signal contribution due to the missing passband in the wavelength region of the
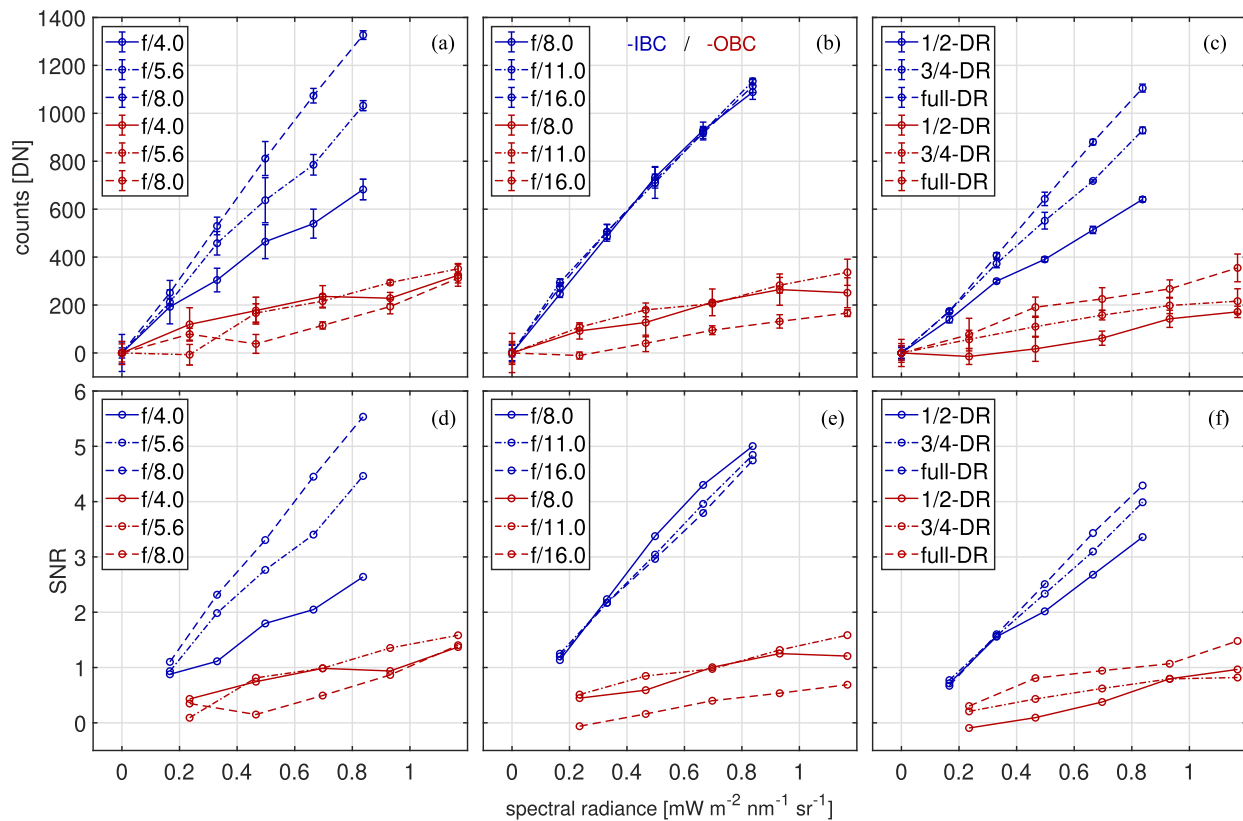
Fig. 8. Derived intensities for IBC (blue) and OBC (red) using, (a) aperture values $f/4.0$, $f/5.6$, and $f/8.0$; (b) $f/8.0$, $f/11.0$, and $f/16.0$; and (c) for half, three-quarter, and full DR and an aperture of $f/11.0$. (d)–(f) Calculated SNR for all three measurement sets. For camera settings see Table II.

outside band filter. From the total resolvable counts, their progression and standard deviations as well as from calculated SNR in Fig. 8(d)–(f), one can say that SIF measurement with the presented system is not possible using OBC only. In this context, Fig. 8 directly indicates the need for the FLD method and the increase in relative signal contribution and SNR for measuring SIF. The influence of the DR of both cameras on the signal resolution was investigated by capturing a series of images with half, three-quarters, and full saturation. The resolved counts and SNR for the images recorded with IBC and OBC using $f/11.0$ are shown in Fig. 8(c) and (f). As expected, higher saturation led to an improvement in the overall number of resolved counts as well as SNR.

B. Experimental Study II: Quantifying the Light Dynamic Adaption of Leaf Photosynthesis During Dark-Light Transition

The experiment was conducted to demonstrate one of the advantages of a snapshot imaging system compared to a point- or imaging-spectrometer. The spatial distribution and temporal dynamic of photosynthetic processes can be displayed at once, by capturing multiple frames per second (frames/s).

1) Experimental Setup: The dark-light transition experiment took place in August 2019 at noon, under a clear sky and direct sunlight conditions. A philodendron leaf was placed at a distance of around 50 cm from the camera, and clamped in a sample holder, to achieve a preferably flat surface. One part of the leaf was covered for 30 min to stimulate

dark-adaption while the rest of the leaf was exposed to direct sun light. The above-described four-stripe reference standard was placed next to the sample holder for irradiance calculation in postprocessing.

Cameras were operated with apertures $f/8.0$ and integration times of 40 ms for the IBC and 9 ms for the OBC. An external hardware-trigger signal was set to capture a series of 200 images with a frame rate of 20 frames/s. The recording was started directly after opening the shading and exposing the dark-adapted part to direct sun light.

2) Results: Images were processed according to steps 1–6 of the developed processing chain (see Section II-E), resulting in 200 SIF maps recorded in 10 s. Fig. 9 shows the calculated SIF map from the first frame of the sequence.

The higher fluorescence emission of the formerly shaded leaf area (ROI 1), compared to the rest of the leaf, is clearly visible. This higher emission is the result of the so-called Kautsky effect, which is characterized by a distinct increase of the SIF emission after a dark-adapted leaf is exposed to direct illumination. The increased SIF emission is followed by a continuous decline until, after a few seconds, a steady-state level is reached. This characteristic curve can be seen in Fig. 10. Average values for the six ROIs highlighted in Fig. 9 are plotted for every frame of the image series. Furthermore, two artifacts are visible in Fig. 9. The first one is the yellow outlines, e.g., at the leaf borders, wrongly showing high SIF signals for these areas. They are caused by the parallax error of the dual-camera system as a consequence
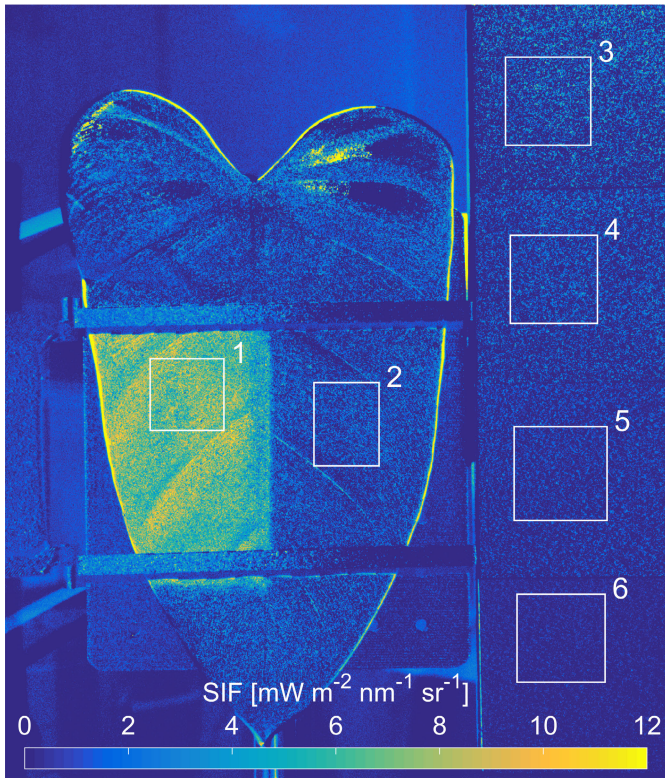
Fig. 9.   SIF map calculated for the first image of the series, instantaneously after exposing the leaf sample to direct sun irradiation. ROIs for a dark-adapted (1) and light-adapted region (2) as well as the four fields of the reflectance target (3)–(6), used for irradiance calculation, are highlighted in white.
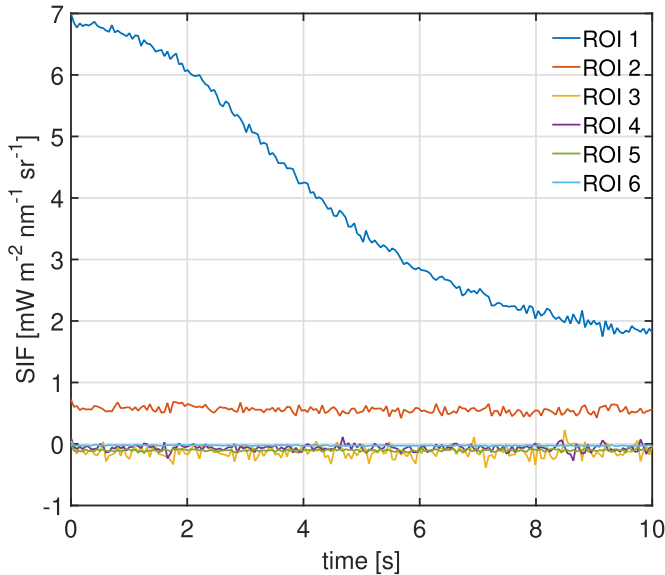

Fig. 10.   Average SIF values of the six ROIs highlighted in Fig. 9 for the entire series of 200 images captured at 20 frames/s.

of the very short object distance and the remaining curvature of the leaf sample. The second artifact is related to the speckle patterns appearing on the reference target (ROIs 3–6). As mentioned before, this pattern can be confused with noise, but clustering does exceed the pixel level as can be seen comparing, e.g., ROI 3 with the background area behind the

top of the leaf. It is worth mentioning that slightly different speckle patterns, regarding their spatial distribution, appear in both channels (OBC and IBC). The effect on the final SIF map that arises from the subtractive combination of both bands, following (1), is not yet finally investigated. Nevertheless, average values for the four target ROIs (3–6) are shown in Fig. 10 indicate that patterns consist of uniformly distributed constructive and destructive interference portions, so that ROI values average to zero. However, from the SIF map in Fig. 9 only, it seems not possible to separate steady-state SIF of the leaf (see ROI 2) from reference target (see ROI 3), due to the low signal compared to speckle contrast. The reason for this is the low saturation level of the sensor, in this case, required to accomplish a frame rate of 20 frames/s.

C. Experimental Study III: Evaluating Image and Signal Quality for a Static Scene Under Natural Illumination Conditions

The experiment was conducted to test the imaging capability of the system for larger object distances, as they would appear, e.g., on a phenotyping platform. In this fixed setup, the integration time was set to meet maximum sensor saturation. The dye fluorescence targets, described in Section II-F2, were placed with either one of the sides up, to increase the visual contrast between fluorescent and nonfluorescent surfaces.

1) Experimental Setup: The measurements were performed on the fourth of February 2021 at 2 P.M. local time under clear sky conditions. Sun elevation angle at the particular day and time, taken from Pysolar [33], was 21° with top-of-atmosphere irradiation of 822 Wm^{-2}. The camera system was mounted on a beam at a height of around 8–9 m, facing in nadir direction, giving a FOV of approximately 4.5 × 4.5 m. Integration times were set to 2 s for the IBC and 200 ms for the OBC, without spatial binning and an aperture of $f/8.0$ for both cameras. The captured image background consisted of mainly short grass with a high amount of moss and a small stony trail. For image processing and analysis, several reference panels were placed within the camera's FOV. To reveal potential disturbances distributed over the image's diagonal field, the reference panels were positioned radially to the top left corner. Fig. 11 shows a subset of the OBC reflectance map with the position and distribution of the reference panels as well as the locations of the ROIs (see Section III).

Due to tree shadows apparent in the top image area (see Fig. 11), ROIs are not covering the full area of every panel. A gray-scale reflectance target (ROI 9) was placed in the image center to enable irradiance calculation in the postprocessing. Besides, three Lambertian reflectance panels (ROIs 1, 2, and 5), and five dye-panels (ROIs 3, 4, 6, 7, and 8) of different sizes were used. After image data acquisition, all postprocessing steps described in Section II-E, except a flatfield correction, were performed. Properties of the used targets are stated in Table III, including which side of the dye panels was facing upward.

2) Results: The calculated, radiometrically calibrated, fluorescence map of the captured image is shown in Fig. 12.

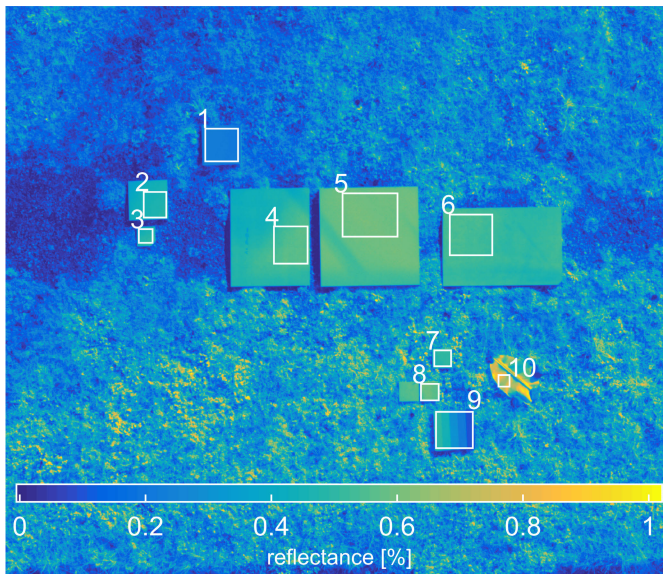Lower SIF emission of the top, shaded part of the image area, compared to the signal derived from the lower,

Fig. 11. Reflectance map for OBC with highlighted ROIs used for analysis. Note that the displayed image is a subset, ROI 9 represents the image center of the originally recorded data.

TABLE III
DESCRIPTION OF THE TARGETS AND AREAS
USED FOR IMAGE ANALYSIS

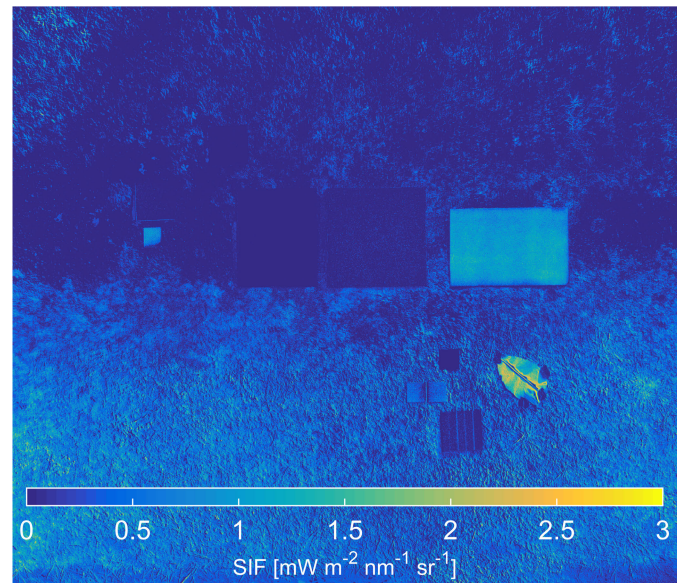| ROI	Target type	Target Properties
1	ZenithLite	R30% (20x20 cm)
2	ZenithLite	R54% (20x20 cm)
3	dye-panel	fluorescent side up
4	dye-panel	fluorescent side down
5	ZenithLite	R54% (50x50 cm)
6	dye-panel	fluorescent side up
7	dye-panel	fluorescent side down
8	dye-panel	fluorescent side up
9	ZenithLite	R50%, R44%, R30%, R21%, R10% (20x20 cm)
10	Banana Leaf	area with medium to high reflectance

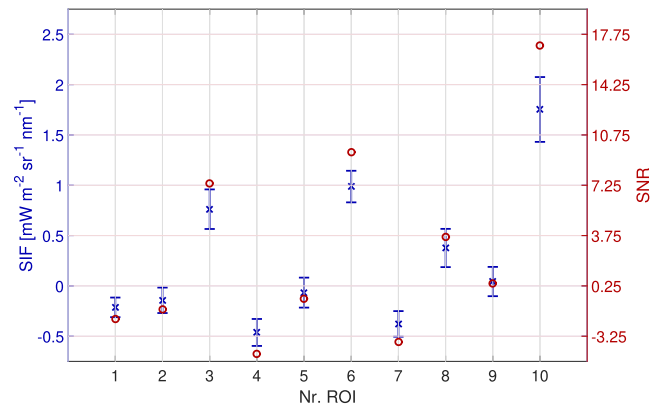Fig. 12. Calculated fluorescence map of the captured scene, showing the same image subset as Fig. 11.

Fig. 13. Mean and standard deviation of the selected ROIs as well as derived SNR, noise fraction is calculated using the standard deviation of a difference image for ROI 5.

sunlit grass area, is noticeable. The SIF signal of the dye-panels (ROIs 3 and 6) with fluorescent side up is clearly visible. The two dye-panels represented by ROI 8 show less contrast compared to the SIF signal from the grass background. Those two panels were used in former experiments and the fluorescent dye may already have degraded, resulting in lower fluorescence emission. All other nonfluorescent targets as well as the trail, show no SIF emission. The banana leaf (ROI 10) provides the highest reflectance as well as SIF values within the image. This observation could be explained by the missing adaption to the full solar spectrum, as it was cut from an indoor plant a few minutes before the experiment. Fig. 13 shows the spatially averaged, emitted SIF of the different ROIs.

The presented SNR in Fig. 13 is comparing the emitted SIF of the particular ROI to the noise fraction derived from ROI 5 as described in Section II-G. ROI 5 was chosen because it is supposed to be the most homogeneous area that was not influenced by shadows. It is worth mentioning that the difference between the noise fraction of the entire image

compared to ROI 5 was only 0.015 mWm^{-2}nm^{-1}sr^{-1}. The gray-scale panel (ROI 9) shows almost zero SIF emission in Fig. 13. The small deviation from zero could be explained by the intersection between each of the panel's stripes. The two 54%-reflectance targets (ROIs 2 and 5) show values slightly below zero. The reason could be the variance in image illumination due to angle-dependent filter transmission (see Section II-B) and the associated lower SIF signal fraction for areas closer to the image borders [see Fig. 3(b)]. The same trend is visible for the two dye targets with the fluorescent side facing down (ROIs 4 and 7). The overall appearance of negative SIF values could be associated with atmospheric and calibration factors [5].

D. Experimental Study IV: Performance Evaluation of the Camera System Installed on a UAV Platform and Comparison of Retrieved SIF to Field Measurements

This experiment was conducted to test the camera system mounted on a UAV under field conditions. The main goal was
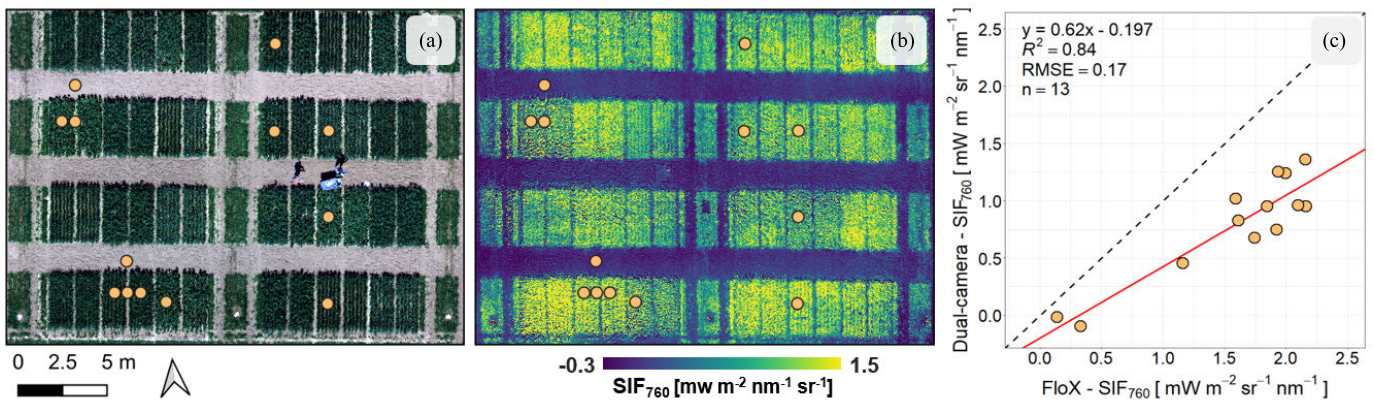
Fig. 14. Results of the first UAV data acquisition. (a) True color composite of the mixed crop breeding experiment using a different camera for spatial orientation. (b) SIF at 760 nm map for the same area derived from image data recorded with the SIF dual-camera system from 25 m above ground level. (c) Scatter plot of SIF at 760 nm measured with the FloX device in the field [orange dots in (a) and (b)] and corresponding SIF values derived from dual-camera image data at the same positions.

to investigate if the camera system provides image data with sufficient spatial accuracy and radiometric quality to produce an ortho-mosaic that forms the basis to derive a SIF map covering a breeding experiment. Simultaneously with the UAV data acquisition, SIF measurements were recorded with a field spectrometer on the ground to verify the accuracy of SIF measured by the dual-camera system.

1) Experimental Setup: The measurements were performed on 13 June 2021 at 1:30 P.M. local time (solar noon) under clear sky conditions at the agricultural research station Campus Klein-Altendorf (CKA) which is affiliated to the Agricultural Faculty of Bonn University, Germany. The camera system was fixed on a DJI Ronin MX gimbal (see Fig. 5) that was mounted on a DJI Matrice Pro 600 (SZ DJI Technology Company Ltd., Shenzhen, China) UAV. Dual-camera image pairs of a mixed-crop breeding experiment (wheat and bean), comprised of numerous plots, each of size 1.5×3 m, were recorded from 25 m above ground level. Sun elevation angle at the particular day and time was $38.5°$ and measured photosynthetic active radiation was 349 Wm^{-2}. The cameras were operated with apertures of $f/8.0$ and integration times of 70 ms for the IBC and 14 ms for the OBC, respectively. The UAV followed a stop-and-go flight pattern only recording image data when hovering above a way point to ensure the acquisition of high-quality image date not affected by motion blur due to long integration times. Image data were recorded with a forward overlap of 80% and a sidelap of 70%. The recorded images were processed using the workflow described in Section II-E. Only the image merging described in step 5 was replaced by using a photogrammetric structure from motion workflow for UAV multicamera arrays in Agisoft MetaShape (Agisoft LLC, St. Petersburg, Russia) to produce an orthomosaic. In parallel to the UAV data acquisition, a FloX point spectrometer (JB Hyperspectral Devices GmbH, Düsseldorf, Germany) was used to record SIF at 760 nm of selected breeding plots [18]. The FloX measures in situ top-of-canopy fluorescence with a FOV of $25°$. The FloX measurements were collected at 2 m above the canopy and used to validate SIF retrieved from the dual-camera orthomosaic.

2) Results: The fluorescence mosaic of the agricultural field experiment is shown in Fig. 14(b). SIF at 760 nm is ranging from -0.3 over soil up to 1.5 $mWm^{-2}nm^{-1}sr^{-1}$ over vegetation with clear variability between experimental plots all comprising healthy vegetation as shown in Fig. 14(a) in the true color representation. The comparison with the ground-based FloX spectrometer reveals a strong relationship with dual-camera SIF ($R^2 = 0.84$, RMSE = 0.17 $mWm^{-2}nm^{-1}sr^{-1}$). However, the dual-camera underestimates SIF compared to ground-based Flox, expressed by a slope of 0.62. The lack of atmospheric correction of the UAV data may explain the underestimation of SIF at 25 m above ground versus 2 m for FloX.

IV. DISCUSSION

In this article, we presented a dual-camera setup combining industrial and scientific components together with established retrieval methods to derive SIF within the O_2A absorption feature. The two most important technical limitations, the narrowband sampling, and cameras' DR, were simulated. Theoretical filter transmission data indicated a four to five times lower radiance for the IBC compared to the OBC, for apertures higher than $f/8.0$ with remaining limitations at the image corners. Regarding the derived suppression factor, an expectable SNR was simulated for either the used sCMOS sensor or a state-of-the-art CMOS sensor used in many current industrial cameras. The experimental data showed good comparability to the simulation, both for band suppression and derived SNR. Results of the first experiment showed that changes in radiance between 0.1 and 0.2 $mWm^{-2}nm^{-1}sr^{-1}$ can be resolved by the camera system under direct sun irradiation. The range of measured radiance for the second, third, and fourth experiments agreed with reported values from the literature. The comparison of the UAV-mounted dual-camera against a ground-based spectroradiometer showed a very good agreement but overall low SIF values likely due to atmospheric effects. Detailed tests of the precision of the derived SIF signal have to be demonstrated in future work. Regarding signal resolution, noise, precision, and SNR, the systems showed lower performance than most cooled spectrometer systems, but an

advantage in spatial and temporal resolution as well as size and weight. Therefore, the systems could be seen as a supplement in combination with airborne remote sensing to measure SIF on different scales and spatial distributions. The high temporal resolution of a snapshot imaging system allows us to measure fast dynamic processes like the Kautsky effect. In a second experiment, the measurement of this effect was demonstrated with a 20 frames/s image series of a dark-adapted leaf. For short integration times (40 ms for the IBC), as used in the second experiment, just a small portion of the camera DR was used. Therefore, SNR was too low to resolve steady-state fluorescence, which is reported to be approximately eight times lower than the maximum fluorescence signal.

V. Conclusion

We could demonstrate that our small-scale SIF camera system can deliver reproducible quantitative data on the intensity of SIF. Even though the camera system cannot compete with cooled spectrometer systems regarding spectral resolution, SNR, and precision of SIF retrieval, the produced numerical values are robust and absolute values are slightly lower than reference values. We did not detect any bias or systematic error in the SIF measurements with the SIF camera system. The slightly lower absolute values are likely related to the SIF FLD retrieval method, which could be empirically corrected in the future. A first comparison against the established SIF measurement system FloX showed good agreement with SIF and a need for atmospheric correction of UAV data. Further measurements should be performed to compare and evaluate the resolved SIF values against imaging spectrometer systems, like HyPlant. Further investigations have to examine the influence of temperature changes on filter transmission characteristics as well as the apparent speckle pattern in near-field measurement. The additional experimental effort is needed to optimize the usable DR of the camera for high-framerate captures. A solution for measurements like this, where short integration times are required, is to reduce spatial resolution by applying pixel binning. This solution enables UAV operation, where short integration times are necessary to ensure image sharpness while recording from a moving platform. First airborne tests on a UAV have been performed and are promising. The SIF camera system may become a valuable complement to ground and airborne sensors by closing a relevant spatial and temporal gap in SIF measurements. We do not see the SIF camera as a stand-alone component within calibration/validation studies, but its spatial resolution, small size and weight, and its versatility have potential, e.g., plant phenotyping experiments, plant breeding studies, small-scale agricultural, and ecosystem monitoring. We are currently working on improving key technical specifications, which may lead to an improvement in the performance of the camera system especially for UAV applications.

References

[1] L. Alonso et al., "Improved Fraunhofer line discrimination method for vegetation fluorescence quantification," *IEEE Geosci. Remote Sens. Lett.*, vol. 5, no. 4, pp. 620–624, Oct. 2008, doi: 10.1109/LGRS.2008.2001180.

[2] L. Alonso and J. Moreno, "A novel portable device to measure leaf reflectance, transmittance and fluorescence emission under natural conditions," in *Proc. 4th Int. Workshop Remote Sens. Vegetation Fluorescence*, Valencia, Spain, 2010, pp. 15–17.

[3] J. Amoros-Lopez et al., "Remote sensing of chlorophyll fluorescence for estimation of stress in vegetation. Recommendations for future missions," in *Proc. IEEE Int. Geosci. Remote Sens. Symp.*, Barcelona, Spain, Jul. 2007, pp. 3769–3772. [Online]. Available: https://ieeexplore.ieee.org/document/4423663

[4] J. Amoros-Lopez et al., "Evaluation of remote sensing of vegetation fluorescence by the analysis of diurnal cycles," *Int. J. Remote Sens.*, vol. 29, nos. 17–18, pp. 5423–5436, Sep. 2008, doi: 10.1080/01431160802036391.

[5] A. Belwalkar, T. Poblete, A. Longmire, A. Hornero, and P. J. Zarco-Tejada, "Comparing the retrieval of chlorophyll fluorescence from two airborne hyperspectral imagers with different spectral resolutions for plant phenotyping studies," in *Proc. IEEE Int. Geosci. Remote Sens. Symp. (IGARSS)*, Jul. 2021, pp. 5845–5848, doi: 10.1109/IGARSS47720.2021.9553265.

[6] J. Bendig, D. Gautam, Z. Malenovský, and A. Lucieer, "Influence of cosine corrector and UAS platform dynamics on airborne spectral irradiance measurements," in *Proc. IEEE Int. Geosci. Remote Sens. Symp.*, Valencia, Spain, Jul. 2018, pp. 8822–8825, doi: 10.1109/IGARSS.2018.8518864.

[7] J. Bendig, Z. Malenovsky, D. Gautam, and A. Lucieer, "Solar-induced chlorophyll fluorescence measured from an unmanned aircraft system: Sensor etaloning and platform motion correction," *IEEE Trans. Geosci. Remote Sens.*, vol. 58, no. 5, pp. 3437–3444, May 2020, doi: 10.1109/TGRS.2019.2956194.

[8] K. Biriukova et al., "Effects of varying solar-view geometry and canopy structure on solar-induced chlorophyll fluorescence and PRI," *Int. J. Appl. Earth Observ. Geoinf.*, vol. 89, Jul. 2020, Art. no. 102069, doi: 10.1016/j.jag.2020.102069.

[9] A. Burkart et al., "A method for uncertainty assessment of passive sun-induced chlorophyll fluorescence retrieval using an infrared reference light," *IEEE Sensors J.*, vol. 15, no. 8, pp. 4603–4611, Aug. 2015, doi: 10.1109/JSEN.2015.2422894.

[10] S. Du et al., "SIFSpec: Measuring solar-induced chlorophyll fluorescence observations for remote sensing of photosynthesis," *Sensors*, vol. 19, no. 13, p. 3009, Jul. 2019, doi: 10.3390/s19133009.

[11] M. J. Firbank, A. Coulthard, R. M. Harrison, and E. D. Williams, "A comparison of two methods for measuring the signal to noise ratio on MR images," *Phys. Med. Biol.*, vol. 44, no. 12, pp. 261–264, Dec. 1999, doi: 10.1088/0031-9155/44/12/403.

[12] C. Frankenberg et al., "The chlorophyll fluorescence imaging spectrometer (CFIS), mapping far red fluorescence from aircraft," *Remote Sens. Environ.*, vol. 217, pp. 523–536, Nov. 2018, doi: 10.1016/j.rse.2018.08.032.

[13] K. Grossmann, C. Frankenberg, T. S. Magney, S. C. Hurlock, U. Seibt, and J. Stutz, "PhotoSpec: A new instrument to measure spatially distributed red and far-red solar-induced chlorophyll fluorescence," *Remote Sens. Environ.*, vol. 216, pp. 311–327, Oct. 2018, doi: 10.1016/j.rse.2018.07.002.

[14] L. Gu, J. D. Wood, C. Y. Chang, Y. Sun, and J. S. Riggs, "Advancing terrestrial ecosystem science with a novel automated measurement system for sun-induced chlorophyll fluorescence for integration with eddy covariance flux networks," *J. Geophys. Res., Biogeosci.*, vol. 124, no. 1, pp. 127–146, Jan. 2019, doi: 10.1029/2018JG004742.

[15] J. A. Plascyk, "The MK II Fraunhofer line discriminator (FLD-II) for airborne and orbital remote sensing of solar-stimulated luminescence," *Opt. Eng.*, vol. 14, no. 4, p. 339, Aug. 1975, doi: 10.1117/12.7971842.

[16] H. Kautsky and A. Hirsch, "Neue versuche zur kohlensäureassimilation," *Die Naturwissenschaften*, vol. 19, no. 48, p. 964, Nov. 1931, doi: 10.1007/BF01516164.

[17] P. H. Lissberger and W. L. Wilcock, "Properties of all-dielectric interference filters. II. Filters in parallel beams of light incident obliquely and in convergent beams," *J. Opt. Soc. Amer.*, vol. 49, no. 2, pp. 126–130, Feb. 1959, doi: 10.1364/JOSA.49.000126.

[18] T. Julitta et al., "Accurate measurements of fluorescence in the O2A and O2B band using the FloX spectroscopy system—Results and prospects," in *Proc. Potsdam GHG Flux Workshop, Photosystems Ecosystems*, Potsdam, Germany, Oct. 2017, pp. 24–26.

[19] A. MacArthur, I. Robinson, M. Rossini, N. Davis, and K. MacDonald, "A dual-field-of-view spectrometer system for reflectance and fluorescence measurements (Piccolo Doppio) and correction of etaloning," in *Proc. 5th Int. Workshop Remote Sens. Vegetation Fluorescence*, Paris, France, Apr. 2014, pp. 1–9. [Online]. Available: https://www.pure.ed.ac.uk/ws/portalfiles/portal/17385047/A_DFOV_spectrometer_system_for_reflectance_and_fluorescence_Piccolo_.pdf

[20] H. A. Macleod, *Thin-Film Optical Filters* (Series in Optics and Opto-electronics), 4th ed. Boca Raton, FL, USA: CRC-Press, 2010, p. 808.

[21] S. W. Maier, "Remote sensing and modelling of solar induced fluorescence," in *Proc. FLEX Workshop (ESA SP-527)*, Noordwijk, The Netherlands, Jun. 2002, p. 6.

[22] K. Maseyk et al., "UAV-based measurements of solar induced fluorescence to gain insight into canopy-level photosynthesis under elevated CO_2," in *Proc. AGU Fall Meeting*, Washington, DC, USA, Dec. 2018, pp. 34–39.

[23] T. S. McKechnie, "Image-plane speckle in partially coherent illumination," *Opt. Quantum Electron.*, vol. 8, no. 1, pp. 61–67, Jan. 1976, doi: 10.1007/BF00620441.

[24] M. Meroni et al., "Remote sensing of solar-induced chlorophyll fluorescence: Review of methods and applications," *Remote Sens. Environ.*, vol. 113, no. 10, pp. 2037–2051, Oct. 2009, doi: 10.1016/j.rse.2009.05.003.

[25] G. H. Mohammed et al., "Remote sensing of solar-induced chlorophyll fluorescence (SIF) in vegetation: 50 years of progress," *Remote Sens. Environ.*, vol. 231, Sep. 2019, Art. no. 111177, doi: 10.1016/j.rse.2019.04.030.

[26] I. Moya, F. Daumard, N. Moise, A. Ounis, and Y. Goulas, "First airborne multiwavelength passive chlorophyll fluorescence measurements over La Mancha (Spain) fields," in *Proc. Recent Adv. Quant. Remote Sens. Conf.*, Torrent, Spain, Sep. 2006, pp. 820–825.

[27] I. Moya, "A new instrument for passive remote sensing1. Measurements of sunlight-induced chlorophyll fluorescence," *Remote Sens. Environ.*, vol. 91, no. 2, pp. 186–197, May 2004, doi: 10.1016/j.rse.2004.02.012.

[28] J. Pacheco-Labrador et al., "Sun-induced chlorophyll fluorescence I: Instrumental considerations for proximal spectroradiometers," *Remote Sens.*, vol. 11, no. 8, p. 960, Apr. 2019, doi: 10.3390/rs11080960.

[29] I. Paynter, B. Cook, L. Corp, J. Nagol, and J. McCorkel, "Characterization of FIREFLY, an imaging spectrometer designed for remote sensing of solar induced fluorescence," *Sensors*, vol. 20, no. 17, p. 4682, Aug. 2020, doi: 10.3390/s20174682.

[30] C. R. Pidgeon and S. D. Smith, "Resolving power of multilayer filters in nonparallel light," *J. Opt. Soc. Amer.*, vol. 54, no. 12, pp. 1459–1466, Dec. 1964, doi: 10.1364/JOSA.54.001459.

[31] A. Porcar-Castell et al., "Linking chlorophyll a fluorescence to photosynthesis for remote sensing applications: Mechanisms and challenges," *J. Experim. Botany*, vol. 65, no. 15, pp. 4065–4095, Aug. 2014, doi: 10.1093/jxb/eru191.

[32] U. Rascher et al., "Sun-induced fluorescence—A new probe of photosynthesis: First maps from the imaging spectrometer HyPlant," *Global Change Biol.*, vol. 21, no. 12, pp. 4673–4684, Dec. 2015, doi: 10.1111/gcb.13017.

[33] I. Reda and A. Andreas, "Solar position algorithm for solar radiation applications," Nat. Renew. Energy Lab., Golden, CO, USA, Tech. Rep. NREL/TP-560-34302, Jan. 2008. [Online]. Available: https://www.nrel.gov/docs/fy08osti/34302.pdf

[34] J. L. Rienstra, "Transformation of filter transmission data for f-number and chief ray angle," *Proc. SPIE*, vol. 3377, pp. 267–275, Aug. 1998. [Online]. Available: https://www.osti.gov/servlets/purl/671892

[35] B. Siegmann et al., "The high-performance airborne imaging spectrometer HyPlant—From raw images to top-of-canopy reflectance and fluorescence products: Introduction of an automatized processing chain," *Remote Sens.*, vol. 11, no. 23, p. 2760, Nov. 2019, doi: 10.3390/rs11232760.

[36] G. M. Smith and E. J. Milton, "The use of the empirical line method to calibrate remotely sensed data to reflectance," *Int. J. Remote Sens.*, vol. 20, no. 13, pp. 2653–2662, Jan. 1999, doi: 10.1080/014311699211994.

[37] J. Q. Vargas et al., "Unmanned aerial systems (UAS)-based methods for solar induced chlorophyll fluorescence (SIF) retrieval with non-imaging spectrometers: State of the art," *Remote Sens.*, vol. 12, no. 10, p. 1624, May 2020, doi: 10.3390/rs12101624.

[38] X. Yang et al., "FluoSpec 2—An automated field spectroscopy system to monitor canopy solar-induced fluorescence," *Sensors*, vol. 18, no. 7, p. 2063, Jun. 2018, doi: 10.3390/s18072063.

[39] Z. Zhang et al., "Assessing bi-directional effects on the diurnal cycle of measured solar-induced chlorophyll fluorescence in crop canopies," *Agricult. Forest Meteorol.*, vol. 295, Dec. 2020, Art. no. 108147, doi: 10.1016/j.agrformet.2020.108147.
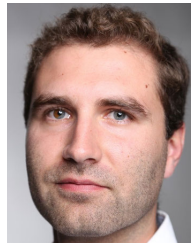
Caspar Kneer was born in Bergisch Gladbach, Germany, in 1985. He graduated in electrical and medical engineering. He received the master's degree in applied physics from the University of Applied Sciences Koblenz, Koblenz, Germany, in 2014.

In the following years, he worked at the Application Center for Multimodal and Airborne Sensors (AMLS), Remagen, Germany. During this time, he has been involved in the development and operation of multispectral camera systems, imaging spectrometers, and equipment for airborne remote sensing, especially in combination with microlight aircraft such as the gyrocopter. From 2018 to 2021, he was working at the Research Centre Jülich (FZJ), Jülich, to develop a compact and drone-compatible imaging system to quantify sun-induced chlorophyll fluorescence.

Andreas Burkart was born in Düsseldorf, Germany, in 1986. He received the Diploma degree in biology from the University of Düsseldorf, Düsseldorf, in 2011, and the Ph.D. degree from the University of Bonn, Bonn, Germany, in association with the Research Centre Jülich, Jülich, Germany, in 2015.

Following a postdoctoral position at the IBG-2 PlantSciences, FZJ, Jülich, Germany, he was one of the founders of JB Hyperspectral Devices GmbH, Düsseldorf, which he currently supports in research, development, and manufacturing. His research interests cover the fields of remote sensing on different scales, hyperspectral instruments, chlorophyll fluorescence, and airships.

Jens Bongartz was born in Neuss, Germany, in 1971. He received the Diploma in physics from the University of Düsseldorf, Düsseldorf, Germany, in 1997, and the Ph.D. degree from the Center of Advanced European Studies and Research (CAESAR), Bonn, Germany, in 2002, on the topic of "Ultrafast Holography."

After two postdoctoral years at CAESAR, he was appointed as a Professor (C3) of Medical and Sensor Engineering at the University of Applied Sciences Koblenz, Koblenz, Germany, in 2004. From 2008 to 2012, he was the Vice President for Research at the University of Applied Sciences Koblenz. From 2012 to 2017, he was the Head of the "Application Center for Multimodal and Airborne Sensors (AMLS)," Remagen, Germany, a cooperation between the University of Applied Sciences Koblenz and the Fraunhofer Institute for High Frequency Physics and Radar Techniques (FHR), Wachtberg. Since 2018, AMLS is a purely in-institute of the university, which he continues to lead. His research focuses on multispectral camera systems, bioelectric sensing, and gyrocopters as a remote sensing platform.

Bastian Siegmann was born in Halle/Saale, Germany, in 1984. He received the Diploma degree in geography from Martin-Luther-University Halle-Wittenberg, Halle, Germany, in 2005, and the Ph.D. degree in remote sensing from the University of Osnabrück, Osnabrück, Germany, in 2017. His dissertation focused on the retrieval of biochemical and structural vegetation parameters from imaging spectroscopy data in preparation for the German hyperspectral satellite mission EnMAP.

Since 2017, he has been a Postdoctoral Researcher at Forschungszentrum Jülich, Jülich, Germany, and he extended his research scope to the retrieval and scaling of remotely-sensed solar-induced chlorophyll fluorescence (SIF) to better understand the physiological response of plants to changing environmental conditions. There, he is responsible for all activities related to the hyperspectral airborne imaging spectrometer HyPlant, which is the official airborne demonstrator for the upcoming FLEX satellite mission of the European Space Agency (ESA), Darmstadt, Germany.

Juliane Bendig was born in Neuss, Germany, in 1985. She received the Diploma degree in geography and the Dr.rer.nat. degree in physical geography from the University of Cologne, Cologne, Germany, in 2010 and 2015, respectively.

From 2011 to 2015, she was a Research Assistant with the University of Cologne. From 2016 to 2019, she was a Research Associate with the University of Tasmania, Hobart, TAS, Australia. In 2020, she was with Centre d'Etudes Spatiales de la Biosphère, Toulouse, France. Since 2020, she has been a Postdoctoral Researcher with the Research Centre Jülich, Jülich, Germany. Her research interests include hyperspectral and chlorophyll fluorescence remote sensing and surface reconstruction with unmanned aircraft systems (UASs), with applications in vegetation studies, mainly in agriculture.

Alexander Jenal was born in Saarlouis, Germany, in 1982. He received the Diploma degree in medical engineering and the master's degree in applied physics from the University of Applied Sciences Koblenz, Koblenz, Germany, in 2008 and 2010, respectively, and the Dr.rer.nat. degree from the University of Cologne, Cologne, Germany, in 2022.

From 2012 to 2017, he was a Research Associate with the "Application Center for Multimodal and Airborne Sensors (AMLS)," Fraunhofer Institute for High Frequency Physics and Radar Techniques (FHR), Remagen, Germany. Since 2018, AMLS is a purely in-institute at the University of Applied Sciences Koblenz, where he is a Research Associate, as well as at the GIS and Remote Sensing Research Group, University of Cologne. His research focuses on the development and application of multispectral imaging systems for vegetation monitoring on crewed and uncrewed aircraft systems.

Uwe Rascher was born in Germany, in 1968. He received the Diploma degree in biology (master's) from University Erlangen-Nürnberg, Erlangen, Germany, in 1996, the Ph.D. degree (Dr.rer.nat.) from the Technical University Darmstadt, Darmstadt, Germany, in 2001, and the Habilitation degree in plant biology from the University of Düsseldorf, Düsseldorf, Germany, in 2009.

From 2001 to 2004, he was working as a Postdoctoral Fellow with the Biosphere 2 Centre, Columbia University, Tucson, AZ, USA. In 2004, he joined the Forschungszentrum Jülich, Jülich, Germany, as a Young Research Scientist, where he was promoted to Group Leader in 2011. In 2014, he was appointed as a Full Professor at the Agricultural Faculty, University of Bonn, Bonn, Germany. He is currently the Head of the research area "Shoot Dynamics" at the Forschungszentrum Jülich, a Principal investigator of the Cluster of Excellence "PhenoRob," and a member of the MAG, European Space Agency (ESA), Darmstadt, Germany, in the preparation of the FLEX satellite mission, which will become the eighth Earth Explorer. His research combines work in plant physiology, remote sensing, ecology, global climate change, and plant phenotyping, and has resulted in 181 peer-reviewed, ISI-listed research articles, including several reviews and high-impact articles (H-index 52). His expertise is in characterizing photosynthesis using chlorophyll fluorescence, hyperspectral reflectance, gas exchange, remote sensing, and image analysis techniques. He further focuses on interdisciplinary work using novel remote sensing approaches to better measure photosynthesis and stress, develop novel plant phenotyping concepts, and model plant-mediated exchange processes from the leaf to the region.